molecules

MDPI

Article

Investigation on Adsorption and Decomposition Properties of CL-20/FOX-7 Molecules on MgH_2(110) Surface by First-Principles

Zhang Yang [1,2], Zhao Fengqi [2], Xu Siyu [2], Yang Fusheng [1,*], Yao Ergang [2], Ren Xiaobing [3], Wu Zhen [1] and Zhang Zaoxiao [1]

1 School of Chemical Engineering and Technology, Xi'an Jiaotong University, Xi'an 710049, China; yangzhang@stu.xjtu.edu.cn (Z.Y.); wuz2015@mail.xjtu.edu.cn (W.Z.); zhangzx@mail.xjtu.edu.cn (Z.Z.)
2 Laboratory of Science and Technology on Combustion and Explosion, Xi'an Modern Chemistry Research Institute, Xi'an 710065, China; zhaofqi@163.com (Z.F.); siyu-zusy99@163.com (X.S.); yaoerg@126.com (Y.E.)
3 Shanxi Northern Xing'an Chemical Industry CO.LTD, Taiyuan 030008, China; 18234065493@163.com
* Correspondence: yang.fs@mail.xjtu.edu.cn

Received: 29 April 2020; Accepted: 28 May 2020; Published: 12 June 2020

Abstract: Metal hydrides are regarded as promising hydrogen-supplying fuel for energetic materials while CL-20 (Hexanitrohexaazaisowurtzitane) and FOX-7 (1,1-Diamino-2,2-dinitroethylene) are typical principal components commonly used in energetic materials. Hence, it is interesting to explore the interactions between them for development of new energetic systems. In this paper, the adsorption and decomposition of CL-20 or FOX-7 molecules on the MgH_2 (110) crystal surface were investigated by employing the First-Principles. In total, 18 adsorption configurations for CL-20/MgH_2 (110) and 12 adsorption configurations for FOX-7/MgH_2 (110) were considered. The geometric parameters for the configurations, adsorption energies, charge transfer, density of states, and decomposition mechanism were obtained and analyzed. In most of the configurations, chemical adsorption will occur. Moreover, the orientation of the nitro-group in CL-20 or FOX-7 with regard to the MgH_2 (110) surface plays an important role on whether and how the energetic molecule decomposes. The adsorption and decomposition of CL-20 or FOX-7 on MgH_2 could be attributed to the strong charge transfer between Mg atoms in the first layer of MgH_2 (110) surface and oxygen as well as nitrogen atoms in the nitro-group of CL-20 or FOX-7 molecules.

Keywords: CL-20; FOX-7; MgH_2; First-Principles; energetic molecule

1. Introduction

With the development of hydrogen energy, various hydrogen storage materials emerge such as metal hydrides. One notable application of metal hydrides is the additive in energetic materials such as solid propellants and explosives [1–6]. Metal hydrides, which are commonly considered as energy carriers for the hydrogen economy [7], have also attracted attention in solid propulsion due to their high chemical energy and remarkable activity [8]. The hydrogen offered by metal hydrides via dehydrogenation reactions is found effective in reducing the relative molecular mass of gas products of combustion, which favours the increase of specific impulses [9,10] for propellants. Furthermore, oxidation of the metal and H_2, which are the products of the dehydrogenation reaction, could also provide a large amount of energy. The metal hydrides could be added into propellants as high energy combustion agents, and the energy level of propellant can be improved. In a previous experimental study by the authors [11], the combustion characteristics were found improved when adding ZrH_2 in a double-base propellant. Similarly, the addition of hydrogen storage materials in explosives can increase

the total energy of explosion [12], and significantly improve the explosive properties of emulsion explosives [13].

In the last few decades, considerable efforts have been devoted to the investigation of metal hydrides [9,14–28] as fuels in energetic materials. Among the various metal hydrides, MgH_2 has the advantages of high hydrogen capacity (7.6wt.%.), abundant resources, little air pollutions after combustion, and good stability (dehydrogenation temperature of 300 °C). Thus, it is paid great attention. The effect of MgH_2 on thermal decomposition performance of cyclortrimethylenetrinitramine (RDX) was researched by Yao et al. [29]. Differential Scanning Calorimetry (DSC) was used to study the thermal decomposition characteristics of RDX with the addition of MgH_2. The results show that MgH_2 decreases the apparent activation energy of RDX from 159.22 kJ/mol to 133.69 kJ/mol. The thermal decomposition behavior of ammonium perchlorate (AP) in the presence of MgH_2 was investigated through DSC by Liu et al. [30]. The results show that 5% MgH_2 can decrease the low and high peak temperatures by 35 °C and 44.2 °C during thermal decomposition of AP, respectively, and increase the apparent heat release of AP from 0.44 kJ × g^{-1} to 1.20 kJ × g^{-1}, which indicates a remarkable catalytic effect of MgH_2 on AP thermal decomposition. The effect of MgH_2 on thermal decomposition process of ammonium nitrate (AN) was studied by Wei et al. [31]. The results show that the addition of MgH_2 makes the initial temperature of decomposition reduce greatly and the decomposition mechanism of AN change.

Although the introduction of metal hydrides into propellants and explosives shows great advantages, the interaction mechanism between metal hydrides and energetic compounds remains unclear due to the huge diversity of both components, which is one key issue restricting the application of metal hydrides in energetic materials. The energy performance of energetic materials is difficult to control without sufficient understanding about the interaction of the concerning components, which causes hidden risks when preparing, using, and storing energetic materials. Unfortunately, many current studies are focused on the effects of metal hydrides addition on the properties of energetic materials through experiments [11–13,29–31], which are costly and hazardous. In this sense, the numerical simulation based on theoretical model provides a reasonable tool to study the interactions among various components in energetic materials. For example, the adsorption and decomposition properties of explosive molecules on the metal surface have been studied theoretically by some scholars. The adsorption and decomposition of RDX, HMX (octahydro-1,3,5,7-tetranitro-1,3,5,7-tetrazocine), and CL-20 molecules on the Al (111) surface [32,33] or FOX-7 on Al_{13} clusters [34] were investigated by Ye et al. employing DFT (density functional theory) calculations. The adsorption and decomposition of the Nitroamine (NH_2NO_2) molecule on Al (111) and Mg (001) surface were studied by Zhou et al. [35,36] from the simulation results of adsorption energy, charge transfer, and adsorption energies of adsorption configurations.

In this paper, the interactions of two typical principal components in energetic materials, i.e., CL-20 and FOX-7, with magnesium hydride were studied by exploring the adsorption and decomposition properties of the energetic molecules on the MgH_2(110) surface. The adsorption configurations, adsorption energies, charge transfer, and density of states before and after the adsorption were calculated by First-Principles simulation, in hope of shedding light on how and why the concerning energetic molecules interact with MgH_2, as well as its significance in preparing for propellants with added metal hydrides.

2. Calculation Method and Model

2.1. Calculation Method

All calculations were performed by employing the CASTEP (Cambridge Sequential Total Energy Package) program [37] with Vanderbilt-type ultrasoft pseudo potentials [38] and a plane-wave expansion of the wave functions in the software package Materials Studio 8.0. General gradient approximation (GGA) was adopted in the exchange and correlation interactions. PBE (the functional

form proposed by Perdew, Burke, and Ernzerhof [39]) was employed. The electronic wave functions were obtained by a density-mixing scheme [40] and the structures were relaxed using the Broyden, Fletcher, Goldfarb, and Shannon method [41]. The cut-off energy was set as 380 eV and the k-point sampling was set as 2 × 2 × 1, which showed good convergence for energy, geometry, and force. When the interatomic interaction force is less than 0.05 eV/Å, the stress is less than 0.1 GPa, the change in atomic energy is less than 2.0×10^{-5} eV/atom, and the change in displacement is less than 0.002 Å. The condition of convergence was deemed to be met. Spin polarization was not considered in the calculation.

2.2. Computational Model

MgH_2 has three crystal morphologies [42,43], and the α-form among them is the most stable at normal temperature, whose (110) face is most stable [44]. Therefore, the computational model employed a 4 × 2 × 1 supercell and a nine-layer MgH_2 (110) surface (as shown in Figure 1). The cell size with a rhombic box of a × b × c was 12.90 Å × 12.04 Å × 30.15 Å.

Five polymorphs, α to ε, are known for CL-20. The ε-polymorph is stable at room temperature and shows the highest density [45]. One ε-CL-20 molecule [46,47] (as in Figure 2) was placed on the upper side of the MgH_2 (110) surface. Two types of nitro groups exist in the CL-20 molecule. The one attached to the six-member ring of CL-20 was represented by type-A, and the other attached to the five-member ring of CL-20, which was represented by type-B (see Figure 2).

1,1-Diamino-2,2-dinitroethylene (FOX-7) is a novel high energetic ingredient [48], whose structure [49,50] was shown in Figure 3. One FOX-7 molecule was placed on the upper side of the MgH_2 (110) surface. Furthermore, 22 Å was taken as the thickness of a vacuum layer in both systems.

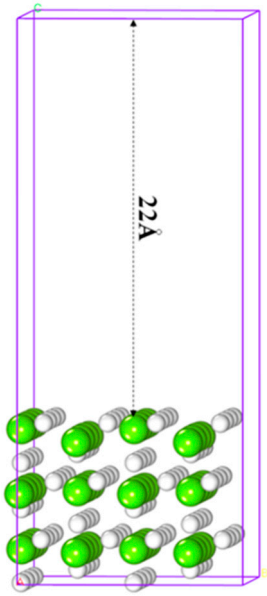

Figure 1. Slab model of MgH_2 (110) where white and green are hydrogen and magnesium atoms, respectively.

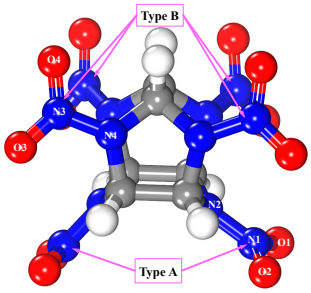

Figure 2. Structure of ε-CL-20 molecule, where white, blue, red, and gray spheres are hydrogen, nitrogen, oxygen, and carbon atoms, respectively.

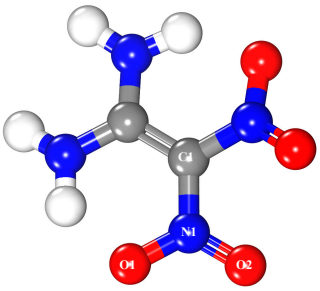

Figure 3. Structure of the FOX-7 molecule where white, blue, red, and gray spheres are hydrogen, nitrogen, oxygen, and carbon atoms, respectively.

3. Calculation Results and Discussion

3.1. Geometries Parameters

The main adsorption sites on the MgH_2 (110) surface are shown in Figure 4, which include Mg-top, H-top, Mg-Mg bridge, H-H bridge, Mg-H bridge, and hole.

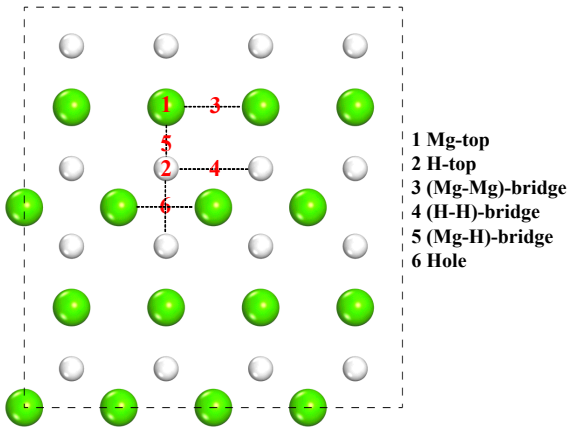

Figure 4. Schematic top view of initial adsorption sites of CL-20 or FOX-7 molecules on the MgH_2 (110) surface.

A total of 18 possible adsorption configurations of CL-20 molecules on the MgH_2 (110) face were considered in the calculation. (1) Type-A nitro group in CL-20 is adsorbed on the MgH_2 (110) surface, and the configurations for the above six sites are signed (a)~(f). (2) Type-B nitro group in CL-20 is adsorbed with the nitro bond perpendicular to the MgH_2(110) surface, and the configurations for the six sites are signed (g)~(l). (3) Type-B nitro group in CL-20 is adsorbed with the nitro bond parallel to the MgH_2 (110) surface, and the configurations for the six sites are signed (m)~(r).

Similarly, 12 possible adsorption configurations for FOX-7 molecules to adsorb on the MgH_2 (110) surface were considered. (1) The nitro group is adsorbed with a nitro bond perpendicular to the MgH_2 (110) surface, and the configurations for the six sites are signed F-V1, F-V2, F-V3, F-V4, F-V5, and F-V6. (2) The nitro group is adsorbed with the nitro bond parallel to the MgH_2 (110) surface, and the configurations for the six sites are signed F-P1, F-P2, F-P3, F-P4, F-P5, and F-P6.

Table 1 shows some important geometrical parameters of the 18 CL-20/MgH_2 configurations, where $r_{(N1–O1)}$ is the bond length between N1 and O1 atoms, and a similar notation applies to $r_{(N1–O2)}$, $r_{(N1–N2)}$, $r_{(N3–O3)}$, $r_{(N3–O4)}$, $r_{(N3–N4)}$. Before the adsorption, $r_{(N1–O1)0}$ = 1.246 **Å**, $r_{(N1–O2)0}$ = 1.245 **Å**, $r_{(N1–N2)0}$ = 1.416 **Å**, $r_{(N3–O3)0}$ = 1.248 **Å**, $r_{(N3–O4)0}$ = 1.253 **Å**, $r_{(N3–N4)0}$ = 1.393 **Å**.

Table 1. Geometrical parameters of the CL-20/MgH_2(110) configurations after adsorption.

Adsorption Configuration	$r_{(N1-O1)}$ (Å)	$r_{(N1-O2)}$ (Å)	$r_{(N1-N2)}$ (Å)	$r_{(N3-O3)}$ (Å)	$r_{(N3-O4)}$ (Å)	$r_{(N3-N4)}$ (Å)
a	1.292	1.299	0	1.268	1.250	1.392
b	1.416	1.465	1.501	1.250	1.248	1.410
c	1.419	1.404	1.535	1.252	1.252	1.407
d	1.405	1.424	1.515	1.257	1.247	1.415
e	1.312	1.320	0	1.258	1.250	1.403
f	1.701	1.342	1.488	1.255	1.247	1.419
g	1.247	1.258	1.410	0	1.286	1.352
h	1.251	1.365	1.397	1.411	1.263	0
i	1.270	1.252	1.405	0	1.279	1.369
j	1.267	1.267	1.386	1.320	1.272	0
k	1.268	1.243	1.395	1.421	1.479	1.453
l	1.273	1.250	1.397	1.381	1.258	0
m	1.255	1.259	1.398	1.301	1.284	0
n	1.244	1.261	1.400	1.329	1.267	0
o	1.253	1.255	1.402	1.325	1.272	0
p	1.263	1.267	1.384	1.325	1.272	0
q	1.266	1.248	1.400	1.325	1.267	0
r	1.252	1.250	1.399	1.384	1.267	0

It can be seen that the closer the nitro group of CL-20 is to the MgH_2 (110) surface, the easier it will be to get the corresponding bonds elongated or ruptured. Besides, there are no bonds rupture or formation in the b, c, d, f, and k configurations, and physical adsorption are deemed to occur. For the rest of the configurations with decomposition, the bond rupture occurs mostly in the mono-N-NO_2.

The geometrical parameters of the 12 FOX-7/MgH_2(110) configurations are shown in Table 2, where similar notations for the bond length in the CL-20/MgH_2 system applies to $r_{(N1–O1)}$, $r_{(N1–O2)}$, and $r_{(C1–N1)}$ in the FOX-7/MgH_2 system. Before the adsorption, $r_{(N1–O1)0}$=1.242 **Å**, $r_{(N1–O2)0}$=1.250 **Å**, and $r_{(C1–N1)0}$=1.416 **Å**. Rupture of the bonds suggesting chemical adsorption occurs in the F-V1, F-V2, F-V5, F-V6, F-P2, and F-P5 configurations. Instead, the physical adsorption occurs in the rest of the six configurations. The bond rupture mainly occurs in the mono-nitro-N-O bond. This is followed by the bis-nitro-N-O bond, and the C-N bond does not rupture at all, which illustrates an increasing stability of the corresponding bonds. In general, the bonds of the FOX-7 molecule show more tendency to rupture the FV-type configurations, which exhibits an impact of nitro-bond orientation on the interaction between FOX-7 and MgH_2.

Table 2. Geometrical parameters of the FOX-7/MgH_2 (110) configurations after adsorption.

Adsorption Configuration	$r_{(N1-O1)}$ (Å)	$r_{(N1-O2)}$ (Å)	$r_{(C1-N1)}$ (Å)
F-V1	0	1.321	1.351
F-V2	0	1.505	1.385
F-V3	1.427	1.417	1.423
F-V4	1.450	1.458	1.429
F-V5	0	1.470	1.369
F-V6	0	0	1.233
F-P1	1.405	1.331	1.381
F-P2	0	1.340	1.330
F-P3	1.516	1.431	1.500
F-P4	1.496	1.435	1.475
F-P5	0	1.258	1.410
F-P6	1.477	1.450	1.483

3.2. Adsorption Energies

The adsorption energies (E_{ad}) of CL20 and FOX-7 molecules on the MgH_2 (110) surface were calculated. E_{ad} is defined as:

$$E_{ad} = E_{slab/molecule} - (E_{slab} + E_{molecule})$$

where the $E_{slab/molecule}$ is the total energy of the adsorption configurations after adsorption. E_{slab} is the single point energy of the MgH_2 (110) surface and E_{slab} = −48267.4eV. The $E_{molecule}$ is the single point energy of the energetic material molecule, E_{CL-20} = −9492.8eV, E_{FOX-7} = −3198.4eV.

For the CL-20/MgH_2 (110) system, adsorption energies E_{ad} for the 18 adsorption configurations are shown in Figure 5.

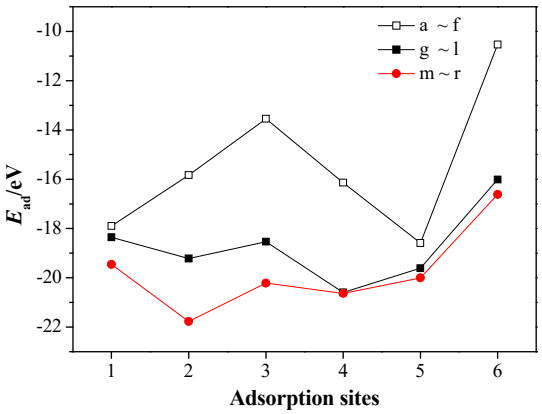

Figure 5. E_{ad} of the CL-20/MgH_2 (110) configurations at different adsorption sites.

In the case of (f) configuration (type-A nitro vertical to hole), whose adsorption energy is the lowest (−10.5 eV), no bond rupture or formation occurs and, hence, physical adsorption is expected. However, in the case of (n) configuration (type-B nitro parallel to H top), whose adsorption energy is the highest (−21.8 eV), the mono-N-NO_2 bond and mono-nitro mono-N-O bond of the type B nitro group rupture, producing NO_2, oxygen atom, and CL-20 fragment. The greater the adsorption energy is, the more intense the corresponding interaction will be. Moreover, we can see that, at the same adsorption sites, the adsorption energies of configurations with type-B nitro adsorbed are generally larger than the configurations with type-A nitro adsorbed. It means that the type-B nitro are easier to adsorb on the MgH_2 (110) surface than type-A nitro. For type-B nitro of CL-20, at the same adsorption sites, the adsorption energies of adsorption configurations where adsorbed nitro of CL-20 is parallel to MgH_2 (110) are larger than the adsorption configurations where adsorbed nitro is perpendicular to

MgH_2 (110). It means that CL-20 molecule is easier to adsorb on the surface of MgH_2 (110) when its nitro group is placed horizontally than being placed vertically.

Meanwhile, the adsorption energies E_{ad} of FOX-7/MgH_2 (110) adsorption configurations are shown in Figure 6. The negative adsorption energies for all the configurations, similar to the CL-20/MgH_2 system, indicate exothermic and stable adsorption [51]. At the six adsorption sites, the adsorption energies of the FV-type configurations are unanimously greater than those of the FP-type configurations, which corresponds to a more stable adsorption. The highest adsorption energy is −21.2 eV when the nitro is vertical to the Mg-H bridge (F-V5 configuration), and the lowest adsorption energy is –15.9 eV when the nitro is parallel to the H-H bridge (F-P3 configuration).

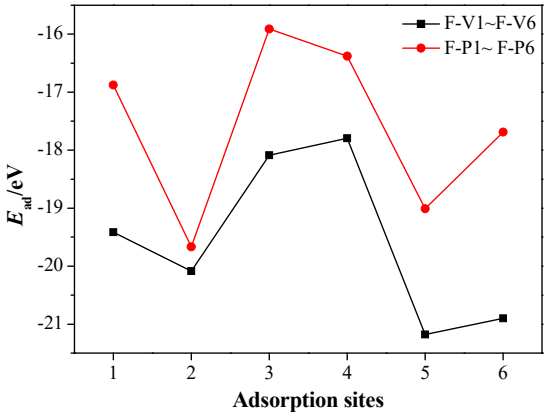

Figure 6. E_{ad} of the FOX-7/MgH_2 (110) configurations at different adsorption sites.

3.3. Charge Transfer of Adsorption Configurations

Electron delocalization and charge transfer induce a chemical reaction of a system. In this section the charge transfer between Mg, H atoms in the first layer of the MgH_2 (110) crystal face, and the activation centers of O and N atoms in the CL-20 or FOX-7 molecules is analyzed. Table 3 lists Mulliken charge distributions of the four types of atoms before and after adsorption. Before adsorption, Mg, H, O_A (the O atoms in type A nitro), O_B (the O atoms in type B nitro), N1, and N3 atoms have charge distribution ranges of 0.98~1.20e, −0.60~−0.60e, −0.34~−0.32e, −0.38~−0.32e, 0.52e, and 0.52e, respectively. After adsorption, the charges of O_A and N1 atoms become significantly more negative in (a)~(f) configurations, while the charges of O_B and N3 atoms become significantly more negative in (g)~(r) configurations, and the charge of Mg atoms is significantly more positive, while the charge of H atoms shows little change, which indicates that strong charge transfer mainly occurs from Mg to O and N atoms in the adsorbed nitro group.

Figure 7 further shows the variation in the Mulliken charge (ΔCharge) of Mg and H atoms in the first layer of the MgH_2(110) crystal face as well as O and N atoms in the CL-20 molecule before and after adsorption. The average charge of Mg atoms, H atoms, O atoms, and N atoms are, respectively, 1.0960e, −0.6000e, −0.3289e, and 0.5266e before adsorption (see the dashed lines in the figure). As can be found, in configurations (a)~(f), the average charge of Mg atoms increases by 0.0296~0.1440e, the average charge of H atoms decreases by 0.0100~0.0306e, the average charge of O_A atoms decreases by 0.2150~0.3075e, and the average charge of N1 atoms decreases by 0.4355~0.5715e. In configurations (g)~(r), the average charge of Mg atoms increases by 0.1284~0.1615e, the average charge of H atoms decreases by 0.0244~0.0350e, the average charge of O_B atoms decreases by 0.1001~0.2375e, and the average charge of N3 atoms decreases by 0.2782~0.55467e. Charge transfer between Mg in the first layer of the MgH_2 (110) crystal face and O, N atoms of the adsorbed nitro group in CL-20 can be confirmed, which leads to the bond rupture in the CL-20 molecule.

Table 3. Charge distribution ranges of Mg and H atoms in the first layer, and the O_A and O_B atoms in the CL-20 molecule of the MgH_2 (110)/CL-20 system before and after adsorption.

Adsorption Configuration	Mg Atoms in the First Layer(e)	H Atoms in the First Layer(e)	O_A Atom(e)	O_B Atom(e)	N1 Atom(e)	N3 Atom(e)
Before adsorption	0.98~1.20	−0.60~−0.60	−0.34~−0.32	−0.38~−0.32	0.52	0.52
a	0.96~1.58	−0.69~−0.57	−0.78~−0.49	−0.53~−0.34	0.04	0.52
b	0.59~1.40	−0.67~−0.58	−0.76~−0.34	−0.37~−0.32	0.05	0.52
c	0.56~1.41	−0.66~−0.59	−0.74~−0.36	−0.38~−0.33	0.09	0.52
d	0.63~1.48	−0.66~−0.54	−0.77~−0.34	−0.52~−0.32	0.05	0.52
e	1.01~1.77	−0.68~−0.57	−0.80~−0.56	−0.42~−0.34	0.05	0.52
f	1.04~1.42	−0.67~−0.59	−0.93~−0.36	−0.44~−0.32	0.07	0.52
g	1.04~1.46	−0.68~−0.57	−0.43~−0.32	−1.27~−0.32	0.52	0.00
h	1.05~1.36	−0.72~−0.58	−0.48~−0.33	−0.80~−0.34	0.52	0.01
i	0.96~1.41	−0.69~−0.58	−0.53~−0.33	−1.29~−0.33	0.52	0.16
j	0.99~1.57	−0.68~−0.59	−0.49~−0.34	−0.78~−0.34	0.52	0.01
k	1.05~1.48	−0.68~−0.56	−0.51~−0.29	−0.76~−0.33	0.52	0
l	1.03~1.77	−0.67~−0.58	−0.51~−0.33	−0.76~−0.34	0.52	0.01
m	1.01~1.50	−0.69~−0.55	−0.43~−0.34	−0.61~−0.34	0.51	0.25
n	1.04~1.45	−0.69~−0.55	−0.46~−0.31	−1.23~−0.32	0.52	0.24
o	0.97~1.56	−0.69~−0.58	−0.40~−0.34	−0.59~−0.33	0.51	0.24
p	1.01~1.47	−0.68~−0.59	−0.50~−0.30	−0.59~−0.33	0.49	0.24
q	1.08~1.48	−0.69~−0.59	−0.49~−0.31	−0.73~−0.33	0.51	0.01
r	0.98~1.58	−0.69~−0.59	−0.40~−0.34	−0.87~−0.33	0.52	0.10

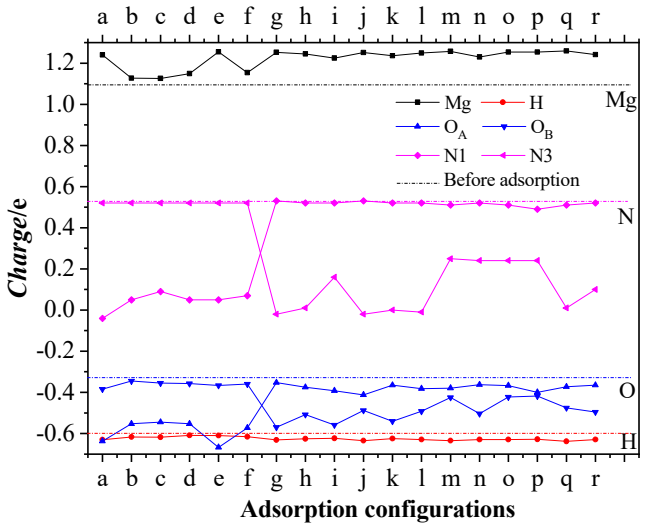

Figure 7. Variation in the average Mulliken charge of Mg and H atoms in the first layer of the MgH_2(110) crystal surface as well as O (O_A and O_B) and N (N1 and N3) atoms in the CL-20 molecule after adsorption. Dash lines are the charge before adsorption.

The charge distribution of Mg and H atoms in the first layer, and the activation center O1, O2, and N1 atoms in the FOX-7 molecule of the FOX-7/MgH_2 (110) system before and after adsorption are shown in Table 4. It can be seen that the charge of Mg atoms is increased after adsorption, while the charges of O1, O2, and N1 atoms are decreased. However, the charges of H atoms and C1 atoms show little changes. Apparently, strong charge transfer mainly occurs between Mg atoms and O, N atoms of the adsorbed nitro group in the FOX-7 molecule.

Table 4. Variation in the average Mulliken charge of Mg and H atoms in the first layer of the MgH_2 (110) crystal surface as well as O1, O2, and N1 atoms in the FOX-7 molecule before and after adsorption.

Adsorption Configuration	Mg Atoms in the First Layer(e)	H Atoms in the First Layer(e)	O1 Atom(e)	O2 Atom(e)	N1 Atom(e)	C1 Atom(e)
Before adsorption	1.10	−0.60	−0.42	−0.32	0.37	0.15
F-V1	1.21	−0.62	−1.27	−0.57	−0.15	0.17
F-V2	1.21	−0.61	−1.31	−0.87	−0.56	0.16
F-V3	1.15	−0.63	−0.71	−0.78	−0.03	0.17
F-V4	1.13	−0.62	−0.80	−0.79	−0.09	0.15
F-V5	1.23	−0.62	−1.26	−0.74	−0.53	0.18
F-V6	1.23	−0.58	−1.26	−1.13	−0.73	0.18
F-P1	1.11	−0.62	−0.70	−0.66	−0.13	0.19
F-P2	1.27	−0.65	−1.22	−0.62	−0.10	0.15
F-P3	1.24	−0.61	−0.79	−0.75	−0.06	0.16
F-P4	1.22	−0.63	−0.80	−0.76	−0.03	0.17
F-P5	1.21	−0.62	−1.29	−1.30	−0.06	0.19
F-P6	1.23	−0.73	−0.66	−0.87	−0.03	0.18

3.4. Density of States of Adsorption Configurations

In order to further investigate the interaction mechanism of the CL-20 or FOX-7 molecule with MgH_2, the density of states (DOS) and partial density of states (PDOS) of the involving systems were analyzed. The DOS of MgH_2, CL-20, and 18 configurations of CL-20/MgH_2 (110), were shown in Figure 8. First, MgH_2 shows DOS around two energy levels, which include −44.7eV~−40.3 eV and −9.2 eV~4.2 eV. The results are close to those reported in Reference [52], verifying the slab model and parameters used. Second, the DOS for the 18 MgH_2/CL-20 configurations are mainly distributed near three energy levels, −44.5~−41.0 eV, −12.1~−0.5 eV, and 0~5.5 eV. In proximity to the Fermi level, the region with the strongest DOS for CL-20 nearly completely coincides with the local DOS for MgH_2, which indicates that the orbits of both are prone to mixing and hybridization. Therefore, the density of states near the Fermi level of all the 18 configurations has intensity significantly higher than those of CL-20 molecules or the MgH_2 (110) crystal face.

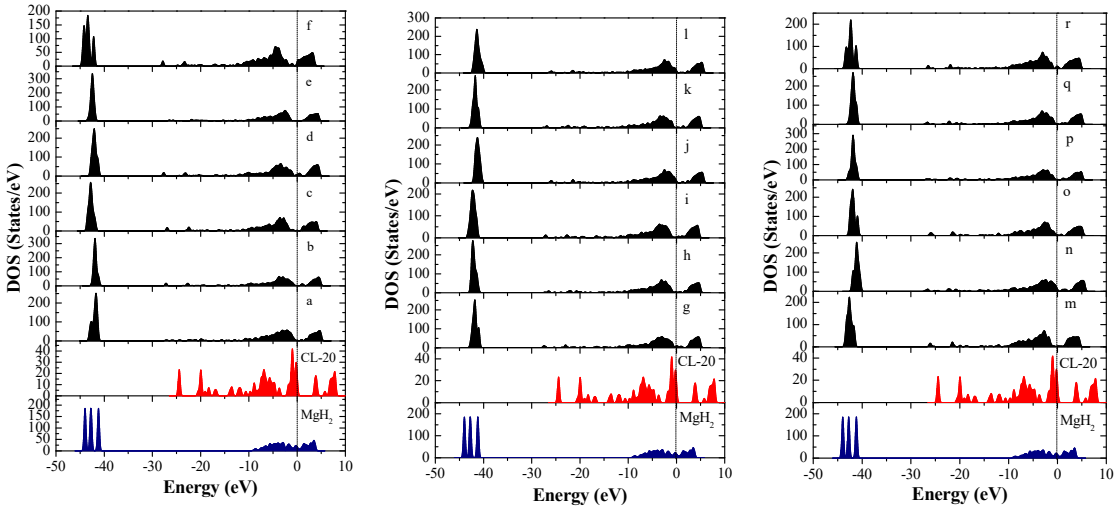

(A) **(B)** **(C)**

Figure 8. Total density of states (DOS) of the MgH_2(110) crystal surface, CL-20 molecule, and CL-20/MgH_2(110) configurations, with a Fermi level denoted by a vertical dashed line, (**A**) (a)~(f) configurations, (**B**) (m)~(r) configurations, and (**C**) (g)~(l) configurations.

Total density of states of Mg and H atoms in MgH_2 (110) slab and the O and N atoms of CL-20 before adsorption are shown in Figure 9. The DOS after adsorption in configurations (g) are shown in Figure 10. We can see that the three peaks of Mg atoms near −44.5~−40.5eV level are merged into one peak because the adsorbed CL-20 molecule causes the breakage of the original periodicity of the crystal structure of magnesium hydride. In addition, the DOS of O and N atoms move toward the lower energy level. Further analysis proves that the density of states of the Fermi level is mainly contributed by p orbits of Mg atoms, p orbits of N atoms, and O atoms of CL-20 molecules. The mixing and hybridization effect of the p orbits enhances the electron delocalization, promotes charge transfer, and, ultimately, leads to decomposition of CL-20 molecules on the MgH_2 (110) crystal face.

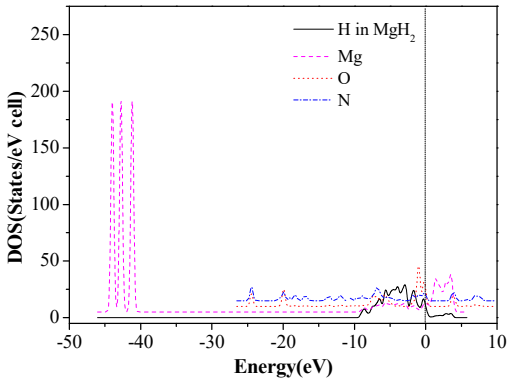

Figure 9. The DOS of Mg, H, O, and N before CL-20 adsorption on the MgH_2 (110) surface.

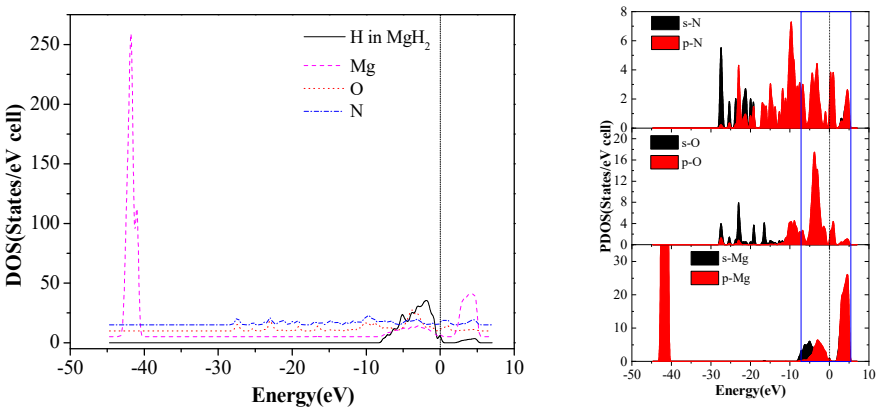

Figure 10. The DOS after adsorption in CL-20/MgH_2(110) configurations (g), (**A**) sum, and (**B**) partial density of states (PDOS).

In order to investigate why the decomposition of FOX-7 on the MgH_2(110) surface is mainly caused by N-O bond rupture, its partial density of states (PDOS) was further investigated. The PDOS of Mg, H, O1, O2, and C1 atoms in F-V1 configurations are shown in Figure 11.

According to PDOS, it can be seen that the p orbital energy of Mg atoms and C1 atoms are located on both sides of the Fermi level, respectively, while the p orbital energy of O1, O2, and N1 atoms crosses the Fermi level. Apparently, Mg, O1, O2, and N1 atoms all have peaks in the vicinity of the Fermi energy levels. In addition, The DOS of Mg, O1, O2, and N1 orbital hybridization is likely to occur, which leads to strong interactions between Mg, O1, O2, and N1 atoms and promotes FOX-7 molecule adsorption on the surface of magnesium hydride. This also confirms the strong charge transfer between Mg and O, N mentioned previously.

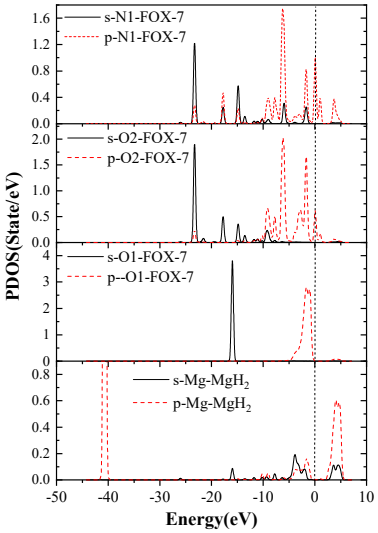

Figure 11. The PDOS of partial atoms in FOX-7/MgH_2 (110) configurations (F-V1).

3.5. Decomposition Mechanisms

Based on the previously mentioned calculations, the decomposition pathways of CL-20 or FOX-7 molecules on the MgH_2(110) surface were obtained.

(I) CL-20 decomposition mechanism

In total, five different decomposition mechanisms have been found for CL-20 (see Figure 12). Since there is more charge transfer between N atoms and Mg atoms than between O atoms and Mg atoms, N-NO_2 is more likely to be ruptured than N-O of nitro when the CL-20 molecule is absorbed on the surface of MgH_2(110).

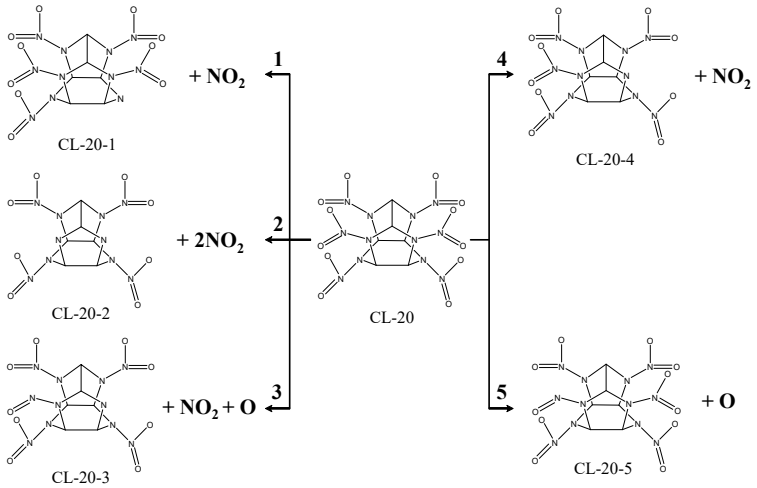

Figure 12. Graph of the decomposition mechanism of CL-20 molecules on the MgH_2(110) face.

(1) The mono-N-NO_2 bond of type A nitro rupture involves the N-NO_2 bond (attaching to type A nitro) in the symmetric position of N1-N2 bond being ruptured, which produces an NO_2 and CL-20-1 fragment. This is applicable to the adsorption configurations of (a), and (e).

(2) The bis-N-NO_2 bond of type B nitro rupture involves the bis-N-NO_2 bond of type B nitro being ruptured, which produces two NO_2 fragments and one CL-20-2 fragment. This is applicable to the adsorption configurations of (m), (o), and (p).

(3) The mono-N-NO_2 bond of type B nitro and mono-nitro mono-N-O bond of type B nitro rupture involves mono-nitro mono-N-O bond of type B nitro being ruptured and producing O.

The mono-N-NO_2 bond of type B nitro is ruptured, which produces an NO_2 and CL-20-3 fragment. This is applicable to the adsorption configurations of (n).

(4) The mono-N-NO_2 bond of type B nitro rupture includes the mono-N-NO_2 bond of type B nitro being ruptured, which produces the NO_2 and CL-20-4 fragment. This is applicable to the adsorption configurations of (h), (j), (l), (q), and (r).

(5) The mono-nitro mono-N-O bond of type B nitro rupture includes the mono-nitro mono-N-O bond of type B nitro being ruptured, which produces the O and CL-20-5 fragment. This is applicable to the adsorption configurations of (g) and (i).

(II) FOX-7 decomposition mechanism

For the decomposition of FOX-7 on the MgH_2(110) surface, three different pathways were found. This is shown in Figure 13.

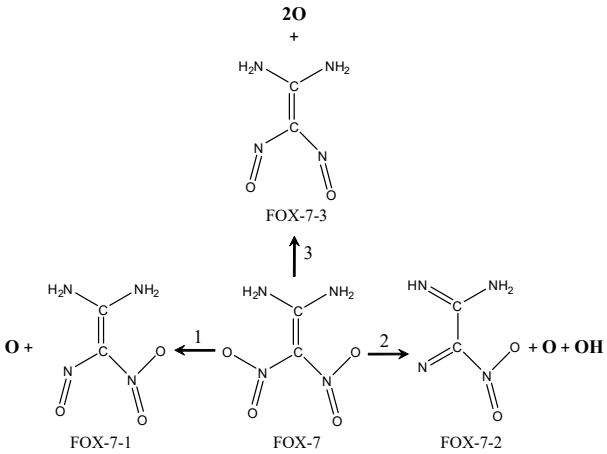

Figure 13. Graph of decomposition mechanism of FOX-7 molecules on the MgH_2(110) surface.

(1) The mono-nitro mono-N-O bond rupture involves the FOX-7-1 fragment and one oxygen atom being formed, which is applicable to F-V1, F-V2, F-V5, and F-P2 configurations.

(2) The mono-nitro bis-N-O bonds, mono-nitro mono-N-O bonds, and mono N-H bond rupture. The FOX-7-2 fragment, one oxygen atom, and one OH are formed, which is applicable to F-V6 configurations.

(3) Bis-nitro mono-N-O bonds rupture. The FOX-7-3 fragment and two oxygen atoms are formed, which is applicable to F-P5 configurations.

In addition, the T-Jump/FTIR combined technology was used to study the thermal decomposition of CL-20/MgH_2 and FOX-7/MgH_2 mixtures with a mass ratio of 1. The microscopic images of MgH_2 samples were obtained (Figure 14) using the field emission scanning electron microscope Carl Zeiss SIGMA. MgH_2 shows a regular spherical shape close to the morphology reported in Reference [29]. The analysis of gas-phase products was carried out using a fast scanning Fourier transform infrared spectrometer (Nicolet 5700FTIR). The interference pattern of incident light was obtained by the Michelson interferometer. The spectral data range was 650 to 4 000 cm^{-1}. The time interval of rapid scanning thermal decomposition process data was 0.125 s. A high-purity argon atmosphere and normal pressure were applied in the experiments. The rapid thermal cracking process of the mixture of CL-20/MgH_2 and FOX-7/MgH_2 were studied under different temperatures and a heating rate of 10 K/min. The NO_2 content in the product of CL-20/MgH_2 and FOX-7/MgH_2 with temperature is shown in Figure 15. At a low temperature under 510.1K, the mixture produces NO_2 with steady low content (less than 5×10^{-13}). Beyond 510.1K, the content of NO_2 increases sharply. The peak value of CL-20/MgH_2 mixture is 2.1×10^{-12} at 540.7 K, and FOX-7/MgH_2 mixture is 1.9×10^{-12} at 594.7 K. CL-20/MgH_2 mixture can produce more NO_2 at a lower temperature than the FOX-7/MgH_2 mixture, which shows higher reactivity for thermal decomposition.

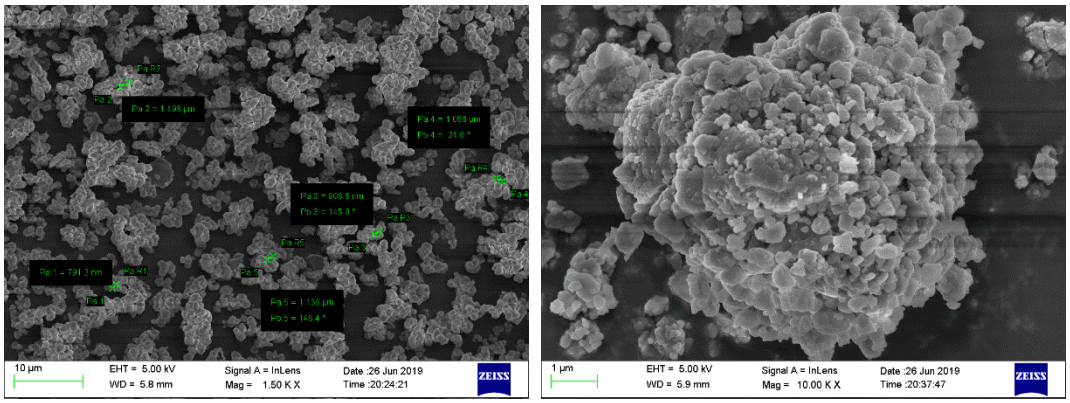

(**A**) (**B**)

Figure 14. SEM images of MgH_2 samples, (**A**) 1.50KX, and (**B**) 10.00KX.

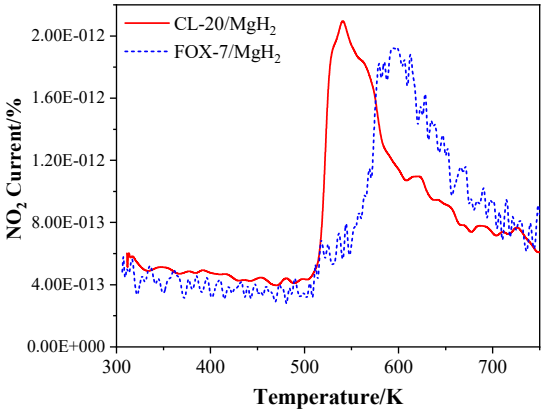

Figure 15. The curve of NO_2 content in the product of the T-Jump/FTIR – MS (mass spectrometry) Analysis of CL-20 or FOX-7 and MgH_2 with temperature.

Combining the simulation and experimental results, better stability of the FOX-7/MgH_2 than CL-20/MgH_2 can be confirmed, which is consistent with the stability comparison between FOX-7 and CL-20 [53,54], and may be attributed to the special π-packing structure and hydrogen bonds of FOX-7 [49]. Furthermore, as pointed out in several previous studies [55–57], CL-20 decomposition generally starts from the fracture of the weakest bonds, i.e., mono-N-NO_2, particularly those connecting the five-member ring and the type-B nitro group [58]. On the other hand, the C-N bond connecting the nitro group in the FOX-7 is relatively stable and not ready for rupture under normal conditions [59]. Such observations could account for the varying tendency of decomposition for adsorptions of type A and B nitro in CL-20 on the MgH_2 (110) surface, and the different products from decomposition of CL-20/MgH_2 and FOX-7/MgH_2.

4. Conclusions

The adsorption and decomposition of CL-20 or FOX-7 molecules on the MgH_2(110) surface were studied in this paper using the First Principles method. The above research showed that:

(1) The bonds of the adsorbed nitro group in energetic molecules are either ruptured or elongated after adsorption, which corresponds to chemical or physical adsorptions, respectively. Negative adsorption energies for all the concerning configurations indicate exothermic and stable adsorption of CL-20 and FOX-7 molecules. The nitro groups attached to the five-member ring of CL-20 (type B nitro) are easier to adsorb on the MgH_2(110) surface than the nitro group attached to the six-member ring of CL-20 (type A nitro). For the type-B nitro, the adsorption is easier to proceed when the corresponding nitro bond is parallel rather than perpendicular to the MgH_2 (110) surface. On the

other hand, chemical adsorption with bond rupture is less likely to take place for FOX-7 than for CL-20, and the configurations with adsorbed nitro perpendicular to the MgH_2 (110) surface show more tendency for decomposition.

(2) The adsorption and decomposition of energetic molecules (CL-20 or FOX-7) on the surface of MgH_2(110) is closely related to the strong charge transfer between Mg atoms in the MgH_2(110) surface and oxygen as well as the nitrogen atoms in the adsorbed nitro group of energetic molecules. Meanwhile, through the DOS of Mg, O, and N, we have found that orbital hybridization is likely to occur near the Fermi energy level, which promotes adsorption of energetic molecules on the surface of MgH_2(110) and the fracture of bonds thereafter.

(3) In total, five decomposition mechanisms of CL-20 on the surface of MgH_2 (110) were determined for the 18 adsorption configurations under discussion in which the rupture of the mono N-NO_2 bond is mostly involved and, hence, the main products contain NO_2, oxygen atoms, and energetic molecule fragments. While for FOX-7/MgH_2 (110) adsorption, three decomposition mechanisms of FOX-7 were found for the 12 adsorption configurations with the main products being oxygen atoms, OH, and FOX-7 fragments.

Author Contributions: Z.Y.—conceptualization, methodology, software, formal analysis, investigation, writing—original draft, visualization; Z.F.—project administration; X.S.—resources, data curation; Y.F.—writing—reviewing and editing, supervision, funding acquisition; Y.E.—software; R.X.—project administration; W.Z.—validation; Z.Z.—data curation. All authors have read and agreed to the published version of the manuscript.

Funding: National Natural Science Foundation of China (No. 21736008) and the open funding of National Defense Key Laboratory on Combustion of Explosives (204-J-2018-0894) financially supported this work.

Conflicts of Interest: The authors declare there is no conflict of interest.

References

1. Yang, Y.J.; Zhao, F.Q.; Yi, J.H.; Luo, Y. Application of hydrogen-storage materials in high-energy solid rocket propellant. *Chin. J. Explos. Propellants* **2015**, *38*, 8–14.
2. Yang, Y.J.; Zhao, F.Q.; Yi, J.H.; Luo, Y. Nanoscale hydrogen-storage materials: Recent progresses and perspectives for applications in propellants. *Chin. J. Energetic Mater.* **2016**, *24*, 194–201.
3. Chen, X.; Zou, J.X.; Zeng, X.Q.; Ding, W.J. Application of Mg-based hydrogen storage materials in energetic materials. *Chin. J. Explos. Propellants* **2016**, *39*, 1–8.
4. Cheng, Y.F.; Liu, R.; Ma, H.H.; Shen, Z.W. Hydrogen storage materials applied in emulsion explosives. *Chin. J. Energetic Mater.* **2013**, *21*, 268–272.
5. Steven, C.S.; Travis, R.S.; Steven, F.S.; Stephen, D.H.; Timothee, L.P. Theoretical performance analysis of metal hydride fuel additives for rocket propellant applications. In Proceedings of the 47th AIAA/ASME/SAE/ASEE Joint Propulsion Conference & Exhibit 31, San Diego, CA, USA, 31 July–3 August 2011.
6. Filippo, M.; Gabriela, G.; Luciano, G.; Luigi, T.D. Theoretical analysis of hydrides in solid and hybrid rocket propulsion. *Int. J. Hydrogen Energy* **2012**, *37*, 1760–1769.
7. Yang, J.; Sudik, A.; Wolvertonb, C.; Siegel, D.J. High capacity hydrogen storage materials: Attributes for automotive applications and techniques for materials discovery. *Chem. Soc. Rev.* **2010**, *39*, 656–675. [CrossRef]
8. Eeward, L.D. Metal-based reactive nanomaterials. *Prog. Energy Combust. Sci.* **2009**, *35*, 141–167.
9. Galfetti, L.; DeLuca, L.; Severini, F.; Colombo, G.; Meda, L.; Marra, G. Pre and post-burning analysis of nano-aluminized solid rocket propellants. *Aerosp. Sci. Technol.* **2007**, *11*, 26–32. [CrossRef]
10. Zhen, F.; Zhou, X.Y.; Zou, M.S.; Meng, L.C.; Yang, R.J.; Wang, L.Q.; Huang, F.L.; Li, J.M. Investigation of the agglomeration reduction mechanism of the aluminized HTPB propellant containing ferric perfluorooctanoate [$Fe(PFO)_3$]. *RSC Adv.* **2019**, *9*, 19031–19038. [CrossRef]
11. Yang, Y.J.; Zhao, F.Q.; Yuan, Z.F.; Ying, W.; An, T.; Chen, X.L.; Xuan, C.L.; Zhang, J.K. On the combustion mechanisms of ZrH_2 in double-base propellant. *Phys. Chem. Chem. Phys.* **2017**, *19*, 32597–32604. [CrossRef]
12. Feng, X.S.; Xu, H.T.; Tian, X.; Feng, X.J. Energy research of explosive containing hydrogen storage alloy. *Chin. J. Energetic Mater.* **2013**, *42*, 13–17.

13. Cheng, Y.F.; Ma, H.H.; Shen, Z.W. Detonation characteristics of emulsion explosives sensitized by MgH_2. *Chin. J. High Press. Phys.* **2013**, *27*, 45–50. [CrossRef]
14. Young, G.; Piekiel, N.; Chowdhury, S.; Zachariah, M.R. Ignition behavior of α-AlH_3. *Combust. Sci. Technol.* **2010**, *182*, 1341–1359. [CrossRef]
15. Luigi, T.; DeLuca, R.; Charles, K.; Volker, W. Ballistic characterization of AlH_3-based propellants for solid and hybrid rocket propulsion. In Proceedings of the 45th AIAA/ASME/SAE/ASEE Joint Propulsion Conference & Exhibit, Denver, CO, USA, 2–5 August 2009.
16. Zhang, W.; Liu, Y.F.; Xie, W.X.; Fan, X.Z.; Xu, H.J.; Liu, X.G. Study on compatibility of AlH_3 with compositions of solid propellant by thermal analysis method. *Chin. J. Explos. Propellants* **2015**, *38*, 41–46. [CrossRef]
17. Gayathri, S.; Reshmi, S. Nitrato Functionalized Polymers for High Energy Propellants and Explosives: Recent Advances. *Polym. Adv. Technol.* **2017**, *28*, 1539–1550. [CrossRef]
18. Liu, L.L.; Xin, J.J.; Ma, F.; Zhi, C.L.; Li, F.S. Preparation of Magnesium-based hydrogen storage materials and their effect on the thermal decomposition of ammonium perchlorate. *Propellants Explos. Pyrotech.* **2013**, *38*, 629–633. [CrossRef]
19. Cao, C.Y.; Lu, S.; Zhang, D.; Gong, L.L.; Zhang, H.P. Effects of nitro guanidine on the thermal behavior and burning characteristics of 5-amino-1H-tetrazole-based propellants. *RSC Adv.* **2017**, *7*, 13808–13816. [CrossRef]
20. Pang, W.Q.; Fan, X.Z.; Zhao, F.Q.; Xu, H.X.; Zhang, W.; Yu, H.J.; Li, Y.H.; Liu, F.L.; Xie, W.X.; Yan, N. Effects of different metal fuels on the Characteristics for HTPB-based fuel rich solid propellants. *Propellants Explos. Pyrotech.* **2013**, *38*, 852–859. [CrossRef]
21. Ding, X.Y.; Shu, Y.J.; Liu, N.; Wu, M.J.; Zhang, J.G.; Gou, B.W.; Wang, H.M.; Wang, C.L.; Dong, S.N.; Wang, W. Energetic characteristics of HMX-Based explosives containing LiH. *Propellants Explos. Pyrotech.* **2016**, *41*, 1079–1084. [CrossRef]
22. Bi, X.L.; Liu, J.P. Detonation properties of high explosives containing ammonia borane. *Z. Anorg. Allg. Chem.* **2016**, *642*, 773–777. [CrossRef]
23. Muddamarri, H.R.; Krishnamurthi, M. Syntheses, characterization and energetic properties of closo-$(B_{12}H_{12})^{2-}$ salts of imidazolium derivatives. *Dalton Trans.* **2013**, *42*, 8854–8860.
24. Paskevicius, M.; Jepsen, L.H.; Schouwink, P.; Černý, R.; Ravnsbæk, D.B.; Filinchuk, Y.; Dornheim, M.; Besenbacher, F.; Jensen, T.R. Metal borohydrides and derivatives—Synthesis, structure and properties. *Chem. Soc. Rev.* **2017**, *46*, 1565–1634. [CrossRef] [PubMed]
25. Frommen, C.; Sørby, M.H.; Heere, M.; Humphries, T.D.; Olsen, J.E.; Hauback, B. Rare Earth Borohydrides—Crystal Structures and Thermal Properties. *Energies* **2017**, *10*, 2115. [CrossRef]
26. Hadjixenophontos, E.; Dematteis, E.M.; Berti, N.; Wołczyk, A.; Huen, P.; Brighi, M.; Le, T.T.; Santoru, A.; Payandeh, S.; Peru, F.; et al. A Review of the MSCA ITN ECOSTORE—Novel Complex Metal Hydrides for Efficient and Compact Storage of Renewable Energy as Hydrogen and Electricity. *Inorganics* **2020**, *8*, 17. [CrossRef]
27. Huang, X.F.; Li, S.J.; Zheng, X.F.; Yang, S.; Guo, Y.H. Combustion mechanism of a novel energetic fuel candidate based on amine metal borohydrides. *Energy Fuels* **2016**, *30*, 1383–1389. [CrossRef]
28. Sakintuna, B.; Lamari-Darkrim, F.; Hirscher, M. Metal hydride materials for solid hydrogen storage: A review. *Int. J. Hydrogen Energy* **2007**, *32*, 1121–1140. [CrossRef]
29. Yao, M.; Chen, L.P.; Du, P.; Peng, J.H. Effect of $Mg(BH_4)_2$ and MgH_2 on thermal decomposition performance of RDX. *China Saf. Sci. J.* **2013**, *23*, 115–120.
30. Liu, L.L.; Li, F.S.; Zhi, C.L.; Song, H.C.; Yang, Y.; Zhang, Q.S. Synthesis of magnesium hydride and its effect on thermal decomposition of AP. *Rare Met. Mater. Eng.* **2010**, *39*, 1289–1292.
31. Wei, Y.J.; Cheng, L.P.; Yao, M.; Peng, J.H. Effect of MgH_2 and $Mg(BH_4)_2$ on thermal decomposition process of ammonium nitrate. *Chin. J. Explos. Propellants* **2015**, *38*, 59–63.
32. Ye, C.C.; Zhao, F.Q.; Xu, S.Y.; Ju, X.H. Adsorption and decomposition mechanism of hexogen (RDX)on Al(111) surface by periodic DFT calculations. *J. Mol. Model.* **2013**, *19*, 2451–2458. [CrossRef]
33. Ye, C.C.; An, Q.; Xu, S.Y.; Ju, X.H. Adsorption and decomposition of HMX andCL-20 on Al(111) surface by DFT investigation. *Surf. Interface Anal.* **2017**, *49*, 441–449. [CrossRef]
34. Ye, C.C.; Zhao, F.Q.; Xu, S.Y.; Ju, X.H. Density functional theory studies on adsorption and decomposition mechanism of FOX-7 on Al_{13} clusters. *Can. J. Chem.* **2013**, *9*, 1207–1212. [CrossRef]

35. Zhou, S.Q.; Zhao, F.Q.; Ju, X.H.; Cheng, X.C.; Yi, J.H. A density functional theory study of adsorption and decomposition of nitroamine molecules on the Al(111) surface. *J. Phys. Chem. C* **2010**, *114*, 9390–9397. [CrossRef]
36. Zhou, S.Q.; Li, D.H.; Zhao, F.Q.; Ju, X.H. A DFT study of adsorption and decompositionofnitroamine molecule on Mg(001) surface. *Struct. Chem.* **2014**, *25*, 409–417. [CrossRef]
37. Segall, M.D.; Lindan Philip, J.D.; Probert, M.J.; Pickard, C.J.; Hasnip, P.J.; Clark, S.J.; Payne, M.C. First-principles simulation: Ideas, illustrations and the CASTEP code. *J. Phys. Condens. Matter* **2002**, *14*, 2717–2744. [CrossRef]
38. Perdew, J.P.; Chevary, J.A.; Vosko, S.H.; Jackson, K.A.; Pederson, M.R.; Singh, D.J.; Fiolhais, C. Atoms, molecules, solids, and surfaces: Applications of the generalized gradient approximation for exchange and correlation. *Phys. Rev. B* **1992**, *46*, 6671–6687. [CrossRef]
39. Perdew, J.P.; Burke, K.; Ernzerhof, M. Generalized gradient approximation made simple. *Phys. Rev. Lett.* **1996**, *77*, 3865–3868. [CrossRef]
40. Dong, W.; Kresse, G.; Furthmuller, J.; Hafner, J. Chemisorption of H on Pd(111): An ab initio approach with ultrasoft pseudo potentials. *Phys. Rev. B* **1996**, *54*, 2157–2166. [CrossRef]
41. Fischer, T.H.; Almlof, J. General methods for geometry and wave function optimization. *J. Phys. Chem.* **1992**, *96*, 9768–9774. [CrossRef]
42. Jain, I.P.; Chhagan, L.; Ankur, J. Hydrogen storage in Mg: A most promising material. *Int. J. Hydrogen Energy* **2010**, *35*, 5133–5144. [CrossRef]
43. Bortz, M.; Bertheville, B.; Böttger, G.; Yvon, K. Structure of the high pressure phase γ-MgH_2 by neutron powder diffraction. *J. Alloys Compd.* **1999**, *287*, 4–6. [CrossRef]
44. Zhang, J.; Hua, M.Y.; Mao, C.; Long, C.G.; Zhou, D.W. First-principles study on structural stability and dehydrogenation thermodynamics of MgH_2 surface. *Chin. J. Nonferrous Met.* **2011**, *2*, 786–792.
45. Van Der Heijden, A.E.D.M.; Bouma, R.H.B. Crystallization and Characterization of RDX, HMX, and CL-Cryst. *Growth Des.* **2004**, *4*, 999–1007. [CrossRef]
46. Huang, C.; Xu, J.J.; Tian, X.; Liu, J.H.; Pan, L.P.; Yang, Z.J.; Nie, F.D. High-yielding and continuous fabrication of nanosized CL-20 based energetic cocrystals via electrospraying deposition. *Cryst. Growth Des.* **2004**, *4*, 2121–2128.
47. Shi, L.; Duan, X.H.; Zhu, L.G.; Liu, X.; Pei, C.H. Directly insight into the inter-and intramolecular interactions of CL-20/TNT energetic cocrystal through the Theoretical Simulations of THz spectroscopy. *J. Phys. Chem. A* **2016**, *120*, 1160–1167. [CrossRef]
48. Latypov, N.V.; Bergman, J.; Langlet, A.; Wellmar, U.; Bemm, U. Synthesis and reactions of 1,1-diamino-2,2-dinitroethylene. *Tetrahedron* **1998**, *54*, 11525–11536. [CrossRef]
49. Sorescu, D.C.; Boatz, J.A.; Thompson, D.L. Classical and Quantum-Mechanical Studies of Crystalline FOX-7(1,1-Diamino-2,2-dinitroethylene). *J. Phys. Chem. A* **2001**, *105*, 5010–5021. [CrossRef]
50. Sun, Q.; Zhang, Y.; Xu, K.; Ren, Z.; Song, J.; Zhao, F. Studies on Thermodynamic Properties of FOX-7 and Its Five Closed-Loop Derivatives. *J. Chem. Eng. Data* **2015**, *60*, 2057–2061. [CrossRef]
51. Chen, Y.H.; Liu, T.T.; Zhang, M.L.; Yuan, L.H.; Zhang, C.R. First Principles Study on the Adsorption of H_2 Molecules on Mg_3N_2 Surface. *Acta Chim. Sin.* **2017**, *75*, 708–714. [CrossRef]
52. Rao, G.N.; Yao, M.; Peng, J.H. First-principles investigation of decomposition and adsorption properties of RDX on the surface of MgH_2. *Chem. Phys.* **2017**, *496*, 15–23. [CrossRef]
53. Fu, X.L.; Fan, X.Z.; Li, J.Z.; Liu, X.G.; Shao, C.B.; Li, H.Y. Research progress on FOX-7. *Sci. Technol. Eng.* **2014**, *14*, 112–119. (In Chinese)
54. Ding, R.Q.; Tao, Y.T.; Xu, J.J.; Sun, J.; Lei, M. Review on crystal structure and properties of energetic compound CL-20 and its cocrystals. *J. Wuhan Univ. (Nat. Sci. Ed.)* **2020**, *66*, 23–31.
55. Okovytyy, S.; Kholod, Y.; Qasim, M.; Fredrickson, H.; Leszczynski, J. The mechanism of unimolicular decomposition of CL-20: A computational DFT study. *J. Phys. Chem. A* **2005**, *109*, 2964–2970. [CrossRef] [PubMed]
56. Wang, X.H.; Zhang, G.; Xie, M.Z.; Liu, N.; Shao, Y.H.; Liu, Z.R. Investigation on thermal decomposition of CL-20 by T-Jump/FTIR. *J. Solid Rocket. Technol.* **2010**, *33*, 675–679. (In Chinese)
57. Macharla, A.K.; Parimi, A.; Anuj, A.V. Decomposition mechanism of Hexanitrohexaazaisowurtzitane (CL-20) by coupled computational and experimental study. *J. Phys. Chem. A* **2019**, *123*, 4014–4020.

58. Liu, Q.; Xiao, J.J.; Chen, J.; Ji, G.F.; Zhu, W.; Zhao, F.; Wu, Q.; Xiao, H.M. Molecular dynamic simulation on sensitivity and mechanical properties of ε-CL-20 crystal at different temperatures. *Chin. J. Explos. Propellants* **2014**, *37*, 7–17.
59. Garmasheva, N.V.; Chemagina, I.V.; Filin, V.P.; Kazakova, M.B.; Loboiko, B.G. Investigation of diaminodinitroethylene (DADNE). In Proceedings of the 7th Seminar "NewTrends in Research of Energetic Materials", Pardubice, Czech Republic, 20–22 April 2004; pp. 116–122.